SENSING OPTICAL FIBERS FOR EARTHQUAKE SOURCE CHARACTERIZATION USING RAW DAS RECORDS

Claudio Strumia[1], Alister Trabattoni[2], Mariano Supino[3], Marie Baillet[2], Diane Rivet[2], Gaetano Festa[1,3]

[1]Università di Napoli Federico II, Physics Department, Complesso Monte S. Angelo, Napoli, Italy.

[2]Université Côte d'Azur, Observatoire de la Côte d'Azur, CNRS, IRD, Géoazur.

[3]Istituto Nazionale di Geofisica e Vulcanologia, Osservatorio Nazionale Terremoti, Roma, Italy.

Corresponding author: Claudio Strumia (claudio.strumia@unina.it)

Key Points:

- A theoretical description of strain far field radiation from a seismic rupture is introduced.
- Source parameters were evaluated from strain data for earthquakes in magnitude range $2.0 - 4.3$
- DAS allows for investigation of source parameters and site effects with fine spatial resolution.

Abstract

Distributed Acoustic Sensing (DAS) is becoming a powerful tool for earthquake monitoring, providing continuous strain-rate records of seismic events along fiber optic cables. However, the use of standard seismological techniques for earthquake source characterization requires the conversion of data in ground motion quantities. In this study we provide a new formulation for far-field strain radiation emitted by a seismic rupture, which allows to directly analyze DAS data

in their native physical quantity. This formulation naturally accounts for the complex directional sensitivity of the fiber to body waves and to the shallow layering beneath the cable. In this domain, we show that the spectral amplitude of the strain integral is related to the Fourier transform of the source time function, and its modelling allows to determine the source parameters.

We demonstrate the validity of the technique on two case-studies, where source parameters are consistent with estimates from standard seismic instruments in magnitude range 2.0 - 4.3. When analyzing events from a 1-month DAS survey in Chile, moment - corner frequency distribution shows scale invariant stress drop estimates, with an average of $\Delta\sigma = (0.8 \pm 0.6)$MPa. Analysis of DAS data acquired in the Southern Apennines shows a dominance of the local attenuation that masks the effective corner frequency of the events. After estimating the local attenuation coefficient, we were able to retrieve the corner frequencies for the largest magnitude events in the catalog.

Overall, this approach shows the capability of DAS technology to depict the characteristic scales of seismic sources and the released moment.

Plain Language Summary

A new formulation for far-field strain radiation from seismic ruptures is derived, leading to a direct interpretation of DAS (Distributed Acoustic Sensing) data to retrieve source properties (seismic moment and source size), via a spectral modelling. This approach is validated on real data recorded in two different tectonic environments, the Chilean margin and the southern Apennines, in Italy. Despite the unique directional sensitivity and peculiar signal characteristics, we demonstrated the high potential of DAS systems in characterizing the seismic ruptures over different space scales, with accuracy increased by redundancy of information from the very-high spatial resolution in the recording of seismic waves.

1 Introduction

Distributed Acoustic Sensing (DAS) is an emerging technology in seismology that allows to get continuous recordings of seismic waves along an optical fiber. DAS systems exploit phase variations in the backscattered light to record the axial strain along the fiber (Hartog, 2017). Thus, a DAS system appears as a single-component seismic array, with main advantage to have a

very dense spatial coverage of sensors and a single endpoint for the collection of data, the interrogator, which sends and receives the laser pulses to measure the strain rate. Also, the availability of existing telecom dark fibers allows to investigate environments usually difficult to monitor, such as oceanic seafloors, volcanic flanks, and geothermal areas, over distances between a few and hundreds of kilometers (e.g., Sladen et al., 2019; Currenti et al., 2021; Tsuji et al., 2021). In the recent years, DAS technology has been successfully applied to seismology for earthquake location (Nishimura et al., 2021; Piana Agostinetti et al., 2022; Sladen et al., 2019), focal mechanism determination (Li et al., 2023), seismic velocity estimation (Lellouch et al., 2019) and site effect characterization (Ajo-Franklin et al., 2019; Spica et al., 2020).

While techniques based on time picking and polarity recognition can be directly applied to strain-rate data, determination of source parameters from DAS measurements requires further development, either processing data directly in the strain-rate domain or converting them into more classical kinematic quantities.

To provide a macroscopic characterization of the source of a seismic event, one needs to determine the seismic moment, the radiated energy, the event size, and the released stress drop, referred to as source parameters. Classical techniques for determination of source parameters are based on the modelling of body wave displacement spectra, that exhibit a flat level followed by a power-law fall-off (Brune, 1970; Madariaga, 1976; Kaneko & Shearer, 2014). Uncertainty in source parameters depends on the knowledge of the Green's function, with a strong correlation between the anelastic attenuation and the source spectral fall-off (Abercrombie, 1995). This correlation can be correctly handled in the computation of uncertainties, using Bayesian approaches (e.g., Supino et al., 2019) or reduced, using small earthquakes as Empirical Green's functions (EGF) (Prieto et al., 2004; Abercrombie & Rice, 2005) or data driven attenuation functions (Oth et al., 2007).

Different approaches have been proposed to apply classical strategies for source parameter estimation to DAS data, converting strain-rate data in ground motion quantities (acceleration, velocity, or displacement). When specific seismic phases dominate the DAS section, acceleration can be directly obtained from strain rate correcting for the apparent phase speed (Daley et al., 2016). The conversion to acceleration of dominant phases can be done using a slant-stack transform, that enables source parameter estimation, even in near real-time for early

warning applications (Lior et al., 2021; 2023). However, only locally dominant phases can be correctly converted with this technique, while energy of smaller amplitude phases is smeared along the seismogram. This issue may become critical for some applications, since DAS data are more sensitive to slow, scattered waves (Trabattoni et al., 2022) and show reduced amplitude for phases travelling at high apparent speeds (Van Den Ende & Ampuero, 2021). Phase independent techniques were also developed for converting strain into ground motion quantities based on F-K rescaling (Wang et al., 2018) and space integration using deformation (Trabattoni et al., 2023). These techniques are sensitive to the rectilinearity of the cable and introduce low-frequency artifacts that must be filtered out. This may affect the low frequency content of seismic spectra and bias the moment magnitude estimation. Nevertheless, they have been shown to provide reliable estimations of Wood-Anderson local magnitude, which requires an accurate displacement measurement above 1 Hz (Trabattoni et al., 2023).

Relative measurements of source parameters can be performed directly in the strain domain using the EGF approach, when the seismic moment of a reference event is available (Chen, 2023). However, this technique is limited to co-located events that differ in magnitude of at least one point (Abercrombie et al., 2017). Alternative approaches exploit correlations between measurements in the strain domain and source parameters. For instance, elastodynamic energy rate from strain was shown to scale with the kinetic energy rate from seismic sensors enabling for magnitude estimation from energy (Trabattoni et al., 2022), while peak strain-rate was demonstrated to correlate with local magnitude (Yin et al., 2023).

In this study we develop a new strategy for computing source parameters in the strain-domain, deriving an analytical formulation that links the source time function with the strain. This formulation allows to evaluate the source parameters inverting strain integral amplitude spectra. The manuscript is organized as follows. In Section 2 we present the new formulation, together with the inversion strategy and the estimation of the average radiation pattern coefficients, that account for the different sensitivity of the along-fiber strain with respect to the displacement. In Section 3, the new technique is validated through an application to real data for two case studies: a 150 km-long fiber offshore Chile and a 1.1 km-long fiber buried in a dry lake inside the Irpinia Near Fault Observatory.

2 Source modelling in strain domain

2.1 Far Field source radiation

Evaluating source parameters from native DAS recordings requires a new formulation that can directly digest dynamic quantities (i.e., strain or strain rate). This formulation can be derived from the far-field radiation emitted by a seismic source and recorded at a receiver at a hypocentral distance r on the Earth's surface.

In a homogeneous medium, the far-field displacement associated with a seismic event and characterized by a source time function $I(t)$ (hereinafter referred to as STF) can be described in spherical coordinates, separating P and S contributions (Haskell, 1964):

$$\begin{aligned} u_r &= \frac{\beta^2}{4\pi\alpha^3 r} sin2\theta cos\phi \; I\left(t - \frac{r}{\alpha}\right) \\ u_\theta &= \frac{1}{4\pi\beta r} cos2\theta cos\phi \; I\left(t - \frac{r}{\beta}\right) \\ u_\phi &= -\frac{1}{4\pi\beta r} cos\theta sin\phi \; I\left(t - \frac{r}{\beta}\right) \end{aligned} \quad (1)$$

Here α and β are the P- and S-wave velocities respectively, while the STF $I(t) = \iint D\left(\xi, t - \frac{r}{c}\right) dS(\xi)$ represents the integral over the fault surface S of the slip function D, which depends on the retarded time due to wave propagation from the source to the receiver (e.g., Sato & Hirasawa, 1973). We assumed a circular crack with fixed slip direction as source model (Madariaga, 1976). The spherical coordinates (θ the colatitude; ϕ the longitude) are defined on a Cartesian reference frame W centered on the fault, where x and z are the along-slip and fault-normal directions, respectively. Here, x and z also represent the directions of the two couples of forces responsible for the earthquake rupture. The three angular functions in equation (1) are indicated respectively as $P(\theta,\phi)_P$, $P(\theta,\phi)_{SV}$, $P(\theta,\phi)_{SH}$, and correspond to the far-field components of the displacement radiation patterns.

We derived equation (1) to evaluate the strain at the receiver (see Supplementary Text S1). Ruling out the contributions that decay faster than $1/r$ (far-field approximation), we obtain:

$$\varepsilon_{rr}^{FF} = \frac{\beta^2}{4\pi\alpha^3 r} P(\theta,\phi)_P \frac{\partial I\left(t-\frac{r}{\alpha}\right)}{\partial r}$$
$$\varepsilon_{r\theta}^{FF} = \frac{1}{8\pi\beta r} P(\theta,\phi)_{SV} \frac{\partial I\left(t-\frac{r}{\beta}\right)}{\partial r} \quad (2)$$
$$\varepsilon_{r\phi}^{FF} = -\frac{1}{8\pi\beta r} P(\theta,\phi)_{SH} \frac{\partial I\left(t-\frac{r}{\beta}\right)}{\partial r}$$

where ε^{FF} is the far-field strain tensor in spherical coordinates. This representation preserves the separation between P and S contributions.

For a homogeneous medium, the radial derivatives of the STF can be written as a function of their time derivatives:

$$\frac{\partial I\left(t-\frac{r}{c}\right)}{\partial r} = -\frac{1}{c}\frac{\partial I\left(t-\frac{r}{c}\right)}{\partial t} \quad (3)$$

where c is the wave velocity of the observed phase. Replacing (3) in (2) and computing the time integral of the strain $\xi = \int \varepsilon dt$, we get

$$\xi_{rr}^{FF} = -\frac{\beta^2}{4\pi\alpha^4 r} P(\theta,\phi)_P I$$
$$\xi_{r\theta}^{FF} = -\frac{1}{8\pi\beta^2 r} P(\theta,\phi)_{SV} I \quad (4)$$
$$\xi_{r\phi}^{FF} = \frac{1}{8\pi\beta^2 r} P(\theta,\phi)_{SH} I$$

In the above equation we omitted the dependence of the STF on the retarded time. For a 1D layered model, this formulation is still a solution of the problem where the velocity c in (3) represents an average velocity beneath the receiver, and (4) becomes (Aki & Richards, 2002):

$$\xi_{rr}^{FF} = -\frac{\beta_S^2}{4\pi\alpha_S^3\alpha_R r}\sqrt{\frac{\alpha_S\rho_S}{\alpha_R\rho_R}} P(\theta,\phi)_P I$$
$$\xi_{r\theta}^{FF} = -\frac{1}{8\pi\beta_S\beta_R r}\sqrt{\frac{\beta_S\rho_S}{\beta_R\rho_R}} P(\theta,\phi)_{SV} I \quad (5)$$
$$\xi_{r\phi}^{FF} = \frac{1}{8\pi\beta_S\beta_R r}\sqrt{\frac{\beta_S\rho_S}{\beta_R\rho_R}} P(\theta,\phi)_{SH} I$$

144 with subscripts S and R indicating that the value is computed at the source and receiver
145 locations.

146 The strain integral is proportional to the STF as for the far-field displacement, enabling
147 for the inversion of ξ amplitude spectra to estimate the source parameters. It is worth to note that
148 equation (5) shows a larger sensitivity of DAS to the shallow velocity structure beneath the
149 cable, as compared to the displacement formulation.
150

151 **2.2 Spectral modelling**

152 To estimate the source parameters, we transformed eq. (5) in the frequency domain, to
153 get the spectral amplitude $\tilde{X}(\omega) = |FFT(\xi(t))|$. Separating the source $\tilde{S}(\omega)$ from the
154 propagation and site effect terms, respectively $\tilde{G}(\omega)$ and $\tilde{Z}(\omega)$, leads to (e.g., Baltay and Hanks,
155 2014):

$$\tilde{X}(\omega) = \tilde{G}(\omega) \cdot \tilde{S}(\omega) \cdot \tilde{Z}(\omega) \tag{6}$$

156 The Green's function $\tilde{G}(\omega)$ for a layered medium and a frequency independent quality
157 factor Q^c can be written as

$$\tilde{G}(\omega) = \widetilde{K}^c A^c e^{-\left(\frac{\omega T^c(r)}{2Q^c}\right)} \tag{7}$$

158 $A^c(r) = 1/r$ is the geometrical spreading contribution and $T^c(r)$ is the source-receiver
159 travel time for the selected phase c. The factor $\widetilde{K}^c$ writes:

$$\widetilde{K}^c = \frac{\bar{B}_c^{FF} F}{8\pi \rho_S^{1/2} \rho_R^{1/2} c_S^{5/2} c_R^{3/2}} \tag{8}$$

160 In the above formula, F is the free surface contribution, ρ the density, also evaluated at
161 the source and receiver locations, and $\bar{B}_c^{FF}$ the mean radiation pattern that averages the
162 directivity effects of the different cable segments along all possible fault orientations. We assume
163 $F = 2$. The radiation pattern is discussed in detail in the next section.

164 For $\tilde{S}(\omega)$ we adopted a generalized Brune model (Brune, 1970):

$$\tilde{S}(\omega) = \frac{M_0}{1 + \left(\frac{\omega}{\omega_c}\right)^{\gamma}} \tag{9}$$

This function depends on the seismic moment M_0, proportional to the plateau level of the spectrum at low frequency, the corner angular frequency ω_c that separates the long wavelengths coherently propagating away from the crack from the interfering small wavelengths, and the decay spectral fall-off γ.

Finally, the site term $\tilde{Z}(\omega)$ was assumed to follow an exponential decay (Anderson & Hough, 1984):

$$\tilde{Z}(\omega) = e^{-\frac{\omega k^c}{2}} \tag{10}$$

where k^c is local attenuation coefficient.

Following Supino et al. (2019), we inverted the amplitude spectra with a probabilistic Bayesian approach (Tarantola, 2004) where the best parameter evaluation and uncertainties come from the integration of the a-posteriori joint Probability Density Function (PDF) in the parameter space. In the general formulation of the inverse problem, we can retrieve up to 5 parameters: the source parameters M_0, $f_c = \omega_c/2\pi$ and γ (f_c is the corner frequency); the regional attenuation factor Q^c and the local attenuation coefficient k^c. The search for maximum of the PDF is performed using a basin-hopping technique on Markov chain paths (Supino et al., 2019).

Correlation exists between the source and propagation parameters of the forward operator used to model the spectra (eqs. 6-10), with model-dependent coefficients (Supino et al., 2019). A formal treatment of the corresponding uncertainty is therefore needed to obtain reliable solutions of the inverse problem (see Abercrombie, 2021 for a complete review). While the probabilistic approach used in this study provides source parameter estimates with uncertainties accounting for between-parameter correlations, the epistemic uncertainty related to the propagation and source time function models clearly affects our estimates.

2.3 Radiation pattern

The average description of the radiation pattern for the displacement (Boore & Boatwright, 1984) cannot be simply extended to fiber recorded strain, due to limited azimuthal

sensitivity of the DAS. The cable allows to recover only one out of the six components of the symmetric tensor ξ, while a three-component instrument provides a complete description of the displacement. In the case of DAS, we averaged the radiation pattern over all the possible fault orientations, and also over all the possible directions of the fiber cable on Earth's surface.

A generic direction of a ray emitted from the source can be described by the take-off and azimuth angles (θ, ϕ), in the reference W centered at the hypocenter. This ray intercepts a portion of the fiber at the Earth surface, whose local orientation can be described by a different couple of angles (θ', ϕ') in the same reference frame W. To account for these new additional degrees of freedom, the average is performed over the focal sphere and all the possible directions of the fiber relatively to the source. This yields:

$$\bar{B}_c^{FF} = \frac{1}{16\pi^2}\int_0^{2\pi}\int_0^{\pi}\int_0^{2\pi}\int_0^{\pi} |A_{1i}P(\theta,\phi)_c A_{j1}^T| sin\theta sin\theta' d\theta' d\phi' d\theta d\phi \quad (11)$$

Here the matrix A accounts for the rotation of the spherical frame from (θ, ϕ) to (θ', ϕ') (see Supplementary Information, Text S2). The terms $P_{ij,c}$ are the angular functions defined in eq. (2). The contributions associated with P and $S = (SV + SH)$ waves can be separated. The integral (11) can be evaluated numerically, leading to:

$$\begin{aligned} \bar{B}_P^{FF} &= 0.2586 \\ \bar{B}_S^{FF} &= 0.2518 \end{aligned} \quad (12)$$

As an example, we show in Figure S1 (Supplementary material) S-wave contributions recorded by fibers oriented along the three-coordinate axes of the reference frame W, as a function of the take-off and azimuth.

3 Data and Results

The proposed technique was applied to evaluate the source parameters on two different datasets. First, we considered DAS data recorded by a 150-km long marine telecommunication cable, located offshore the Chilean margin; then we applied the same technique to earthquakes recorded by a 1.1 km-long cable deployed in the Southern Apennines (Italy).

3.1 Submarine DAS data offshore Chile

DAS data in Chile were recorded during the month of November 2021, when an interrogator unit (OptoDAS – Alcatel Submarine Networks) was connected to a submarine fiber optic telecom cable, operated by the GTD group and linking Concón to La Serena. The DAS was able to sense 150km-long portion of the cable. A map of the cable is represented in Figure 1b and in Figure S3 of Supplementary Information. Data were processed using a gauge length of 8.16 m with a repetition rate of 625 Hz and a spatial sampling of 1.02m averaged over 4.08m. They were further decimated to a sampling rate of 125 Hz and a spatial sampling of 65.28m. In Figure 1a an example of DAS recording along the cable is shown for a $M_L 2.9$ event occurred at $23km$ depth, at minimum and maximum distances from the cable of $24km$ and $93km$ respectively (ID: 20211119T055900, see Data availability statement for catalog reference), along with a zoom on a strain rate record from a single channel.

For the analysis, we focused on a subset of 55 events, whose local magnitude M_L ranges between 2.5 and 4.3, also recorded by the seismic network from the Centro Sismologico National (CSN). These events are representative of the magnitude and distance ranges of earthquakes occurred during the period of the experiment. Origin times from CSN catalog were used as reference times to create three-minute-long DAS records.

We individuated the S-wave arrival time on single traces using the machine learning algorithm Earthquake Transformer - EqT (Mousavi et al., 2020). The associator GaMMA (Zhu et al., 2022) was then applied to evaluate the consistency of the S-picks along the fiber, based on the apparent wave velocity. Examples of automatic picking and detection on DAS data are shown in Supplementary Information Text S3). Accuracy on the picks was shown to be sufficient for extraction of the S window for spectral analysis (Scotto di Uccio et al., 2023). The study focused on the inversion of S phase, which represents the dominant contribution since horizontally deployed fibers are less sensitive to P wave phases owing to their high apparent velocities (Papp et al., 2017; Trabattoni et al., 2022). Moreover, in sedimentary areas, the P-wave train is generally polluted by S-waves converted at the bedrock/sediment interface (Trabattoni et al., 2023).

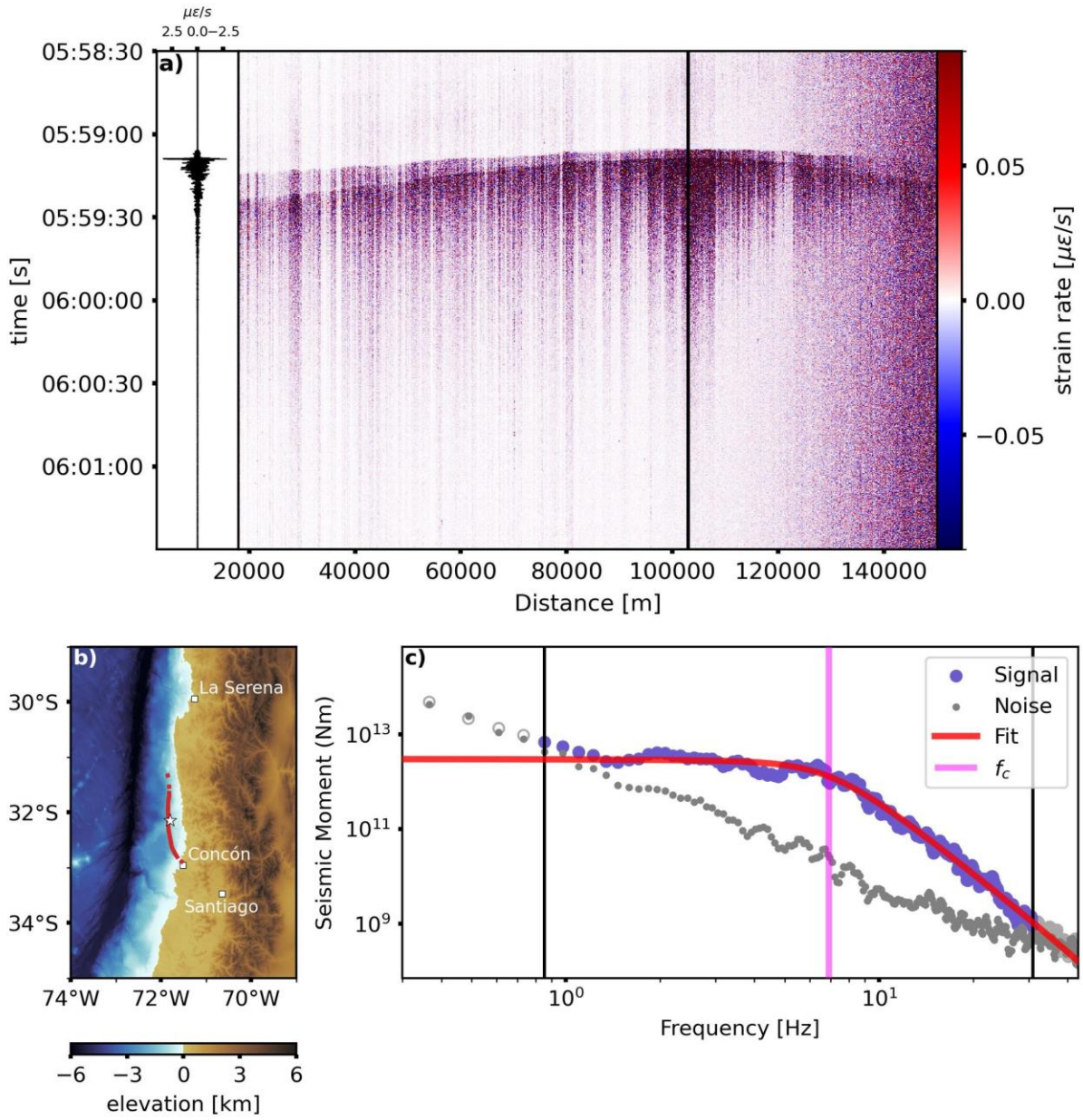

Figure 1: (a) Space-time representation of the strain rate wavefield, bandpass filtered between 1 and 30 Hz, recorded at the fiber for a M_L2.9 event occurred on the 2021/11/19. The black line marks the channel, whose time signal is shown on the left side. **(b)** Event location (yellow star) with respect to the fiber section used in the analysis (filled red curve). **(c)** S-wave spectrum of the selected channel (blue points, gray open circles) and of the noise (gray points) are represented. The vertical black lines individuate the frequency domain where the SNR is larger than the selected threshold and the inversion was performed. The red curve is the best-fit spectrum obtained from the inversion. The flat level at low frequencies indicates seismic moment estimate M_0 at the channel, while the magenta line marks the corner frequency f_c.

Before inversion, data were band pass filtered between $0.05Hz$ and $40Hz$ to mitigate the influence of low frequency oceanic noise and high frequency sources of noise, and then the highest quality channels along the cable were selected based on their Signal to Noise Ratio (SNR). This latter quantity was evaluated by computing the ratio between the 90th percentile of the amplitude in a 6s window after the S arrival time, and the 90th percentile of the amplitude in a noise window of 20s before the origin time of the event. We selected channels with SNR>4, and we processed events only if the number of available channels was larger than 200, that represents almost one tenth of the total number of channels. Following this approach, we were able to estimate the source parameters for 37 events. A map of these events is represented in Figure S3 of Supplementary Information.

To model the spectral amplitude expressed in eq. (8) we used $c_S = 4500\ \mathrm{m/s}$ and $Q = 800$ as provided by the tomographic model of Marot et al., (2014). Also, we set $\rho_S = \rho_R = 2700\ \mathrm{kg/m^3}$ and the S-velocity at the receiver $c_R = 400\ \mathrm{m/s}$, according to the analysis of f-k diagrams. For this dataset, we did not observe a saturation of the corner frequency at low magnitudes and thus we considered negligible the site contribution of eq. (10). The length of the signal used to evaluate the spectra depends on the event magnitude, to consider the size dependence of the source duration (Trifunac & Brady, 1975; Supplementary Information Text S5). This window also contains a small portion (10%) of signal before the S-pick to account for uncertainties in arrival times.

In Figure 1c we represent the amplitude spectrum of a channel from the DAS records (See supplementary Information Text S6 for more examples). The signal exhibits a clear plateau level at low frequencies and a decay in the high frequency band. For each channel the inversion is performed in a specific frequency band (delimited in the figure by the vertical black lines), where the spectral amplitude of the signal overcomes the noise of a factor larger than 3.5. Low SNR typical of DAS recordings (Lellouch et al., 2020) results in narrower frequency band to be used for the inversion, as compared to standard seismic instruments.

Seismic moments and corner frequencies evaluated from the selected dataset exhibit near to constant stress drop (Figure 2a). Using the relationship from Keylis-Borok, (1959):

$$\Delta\sigma = \frac{7}{16}\left(\frac{f_c}{C_k\beta}\right)^3 M_0 \tag{13}$$

and the geometrical factor of $C_k = 0.26$ from Kaneko & Shearer (2014), the averaged stress drop was estimated to $\Delta\sigma = (0.8 \pm 0.6)$MPa, which is comparable to what found for earthquakes in central Chile (Şen et al., 2015). We also compared moment magnitude estimations with those obtained from the inversion of seismic records from on land CSN stations. We found great coherency between estimates (Figure 2b). This indicates that the observed plateau level at low frequencies is representative of the event moment release and is not significantly affected by instrumental effects. Furthermore, we also compared moment magnitude obtained from DAS data with local magnitudes from CSN catalog (Supplementary Information Text S7; Figures S6) showing that our estimations are consistent with M_L and that for this range of magnitudes the low frequency plateau is coherent with the energy content of the signal.

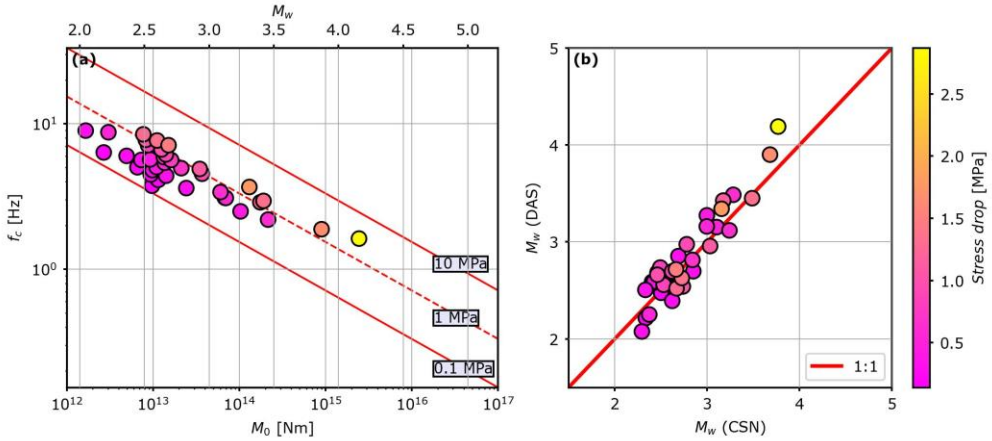

Figure 2: (a) Corner frequency as a function of the seismic moment for the Chilean dataset, exhibiting almost constant stress drop scaling, with average value of (0.8 ± 0.6)MPa and values ranging between 0.1 MPa and 3 MPa. **(b)** Comparison between DAS and CSN moment magnitudes; CSN Mw are obtained from inversion of seismic records from in land stations for the same dataset. Estimations exhibit a scaling consistent with a 1:1 relationship.

The consistency of the modeling of the amplitude decay with the event distance could be asserted by taking advantage of the dense spatial sampling provided by the DAS technology. For each event, we computed the residuals for both M_w and f_c at each channel, by removing the average value estimated for the whole cable from the single channel estimate. We grouped residuals by hypocentral distances in bins of 1 km (from 20 to 150 km) regardless of the event or channel. The median and standard median absolute deviation (SMAD) for residuals were computed for each bin as a function of the hypocentral distance (Figure 3). The estimations are unbiased in the whole distance range. Only for distances below $40km$ the moment magnitude

exhibits residuals slightly larger than zero; this overestimation of the geometrical spreading correction could be ascribed to possible uncertainty in event location.

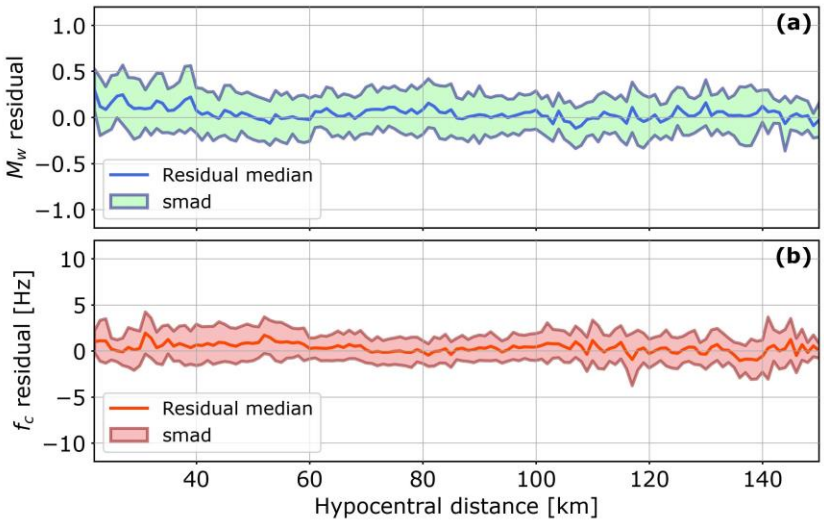

Figure 3: Analysis of the source parameters residuals as a function of the hypocentral distance. Bold lines represent the median of the residuals for each distance bin, while the error is represented by the Standard Median Absolute Deviation (SMAD). **(a)** M_w residuals exhibit a slight bias at short distances (<40 km), while no other trend is evident at other distances. **(b)** f_c residuals are unbiased, showing that the exponential decay as a model for regional attenuation well describes the spectral decay for a wide range of hypocentral distances.

The possibility of evaluating source parameters at thousands of different stations comes with variability of spectral fits and thus in source parameter evaluations, as shown in Figure 3, as consequence of both propagation and different coupling conditions along the cable (See Supplementary Information Text S8, Figure S7).

3.2 Southern Apennines DAS measurements

In contrast to Chilean events, the Southern Italy DAS survey focused on smaller microseismic events ($M_L \leq 2.5$), that represent a challenging test for the resolution of source parameters. The data were acquired during a 5-month experiment, involving a DAS interrogator (Febus A1-r) connected to a 1.1km-long L-shaped fiber optic cable, buried into a shallow trench ($0.3\text{m} - 1.0\text{m}$) in a dry lake near the town of Colliano (Figure 4b). The instrument was set to work with a sampling rate of 200Hz, further downsampled to 100Hz, and a spatial sampling of 2.4m, with a gauge length of 4.8m (more details in Trabattoni et al., 2022).

The site of the installation was near the emergence of the main segment of the normal fault system that generated the devastating 1980 $M6.9$ Irpinia earthquake in the Southern Apennines. The area is nowadays monitored by the Irpinia Near Fault Observatory (INFO), (Chiaraluce et al., 2022) that detected several dozens of events during the deployment period.

Figure 5 shows the recordings of a $M_L 2.3$ event occurred on 2021/09/20 at 13:07:55 and reveals the specific propagation pattern due to the shallow sedimentary layering, as described in Trabattoni et al. (2022).

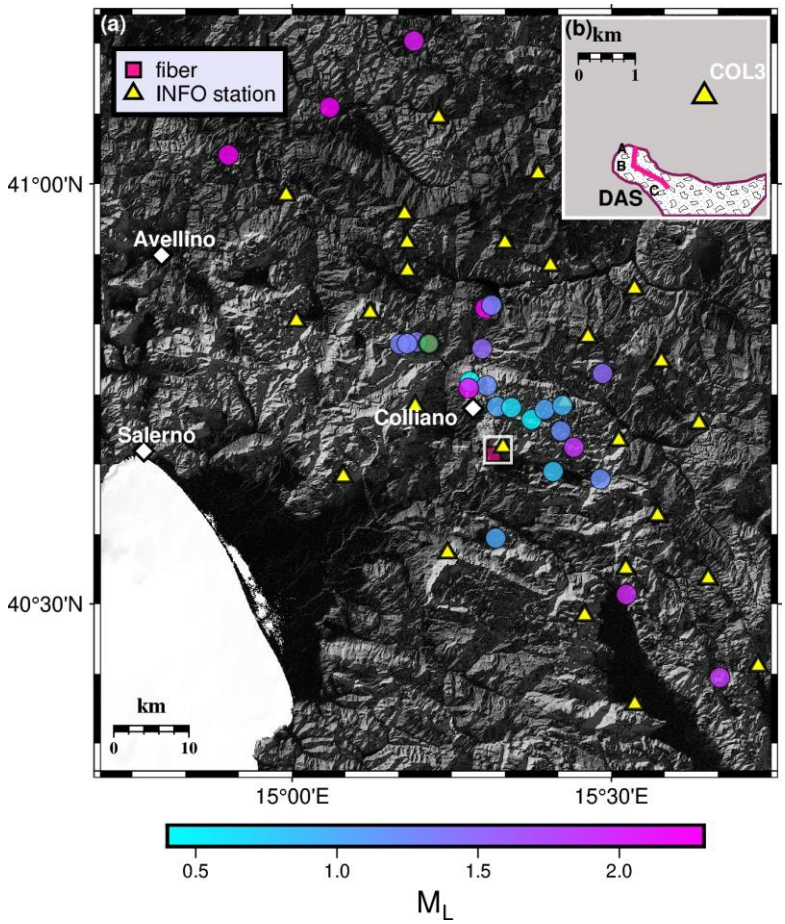

Figure 4*:* (a) Map showing the location of the fiber (white square) and the events recorded by the DAS interrogator (color code based on their M_L). The green point marks the event represented in Figure 5 (almost $20km$ away from the installation site). Panel **(b)** depicts the area contained in the white square, showing the L-shaped fiber (magenta line), with a kink in B, and the nearest INFO station COL3 (yellow triangle), located at less than $2km$ from the interrogator. The white-pattern area represents the dry lake where the cable was buried for the experiment.

As for the Chilean dataset, we considered events in the local bulletin and extracted related DAS waveforms from the continuous data stream. We limited our analysis to the

channels of the section AC, excluding few low-quality channels at the beginning and the end of the cable. Data were filtered between $0.1Hz$ and $30Hz$ to isolate the earthquake signal from environmental and anthropogenic noise and to perform a SNR based channel selection as previously described for the Chilean case.

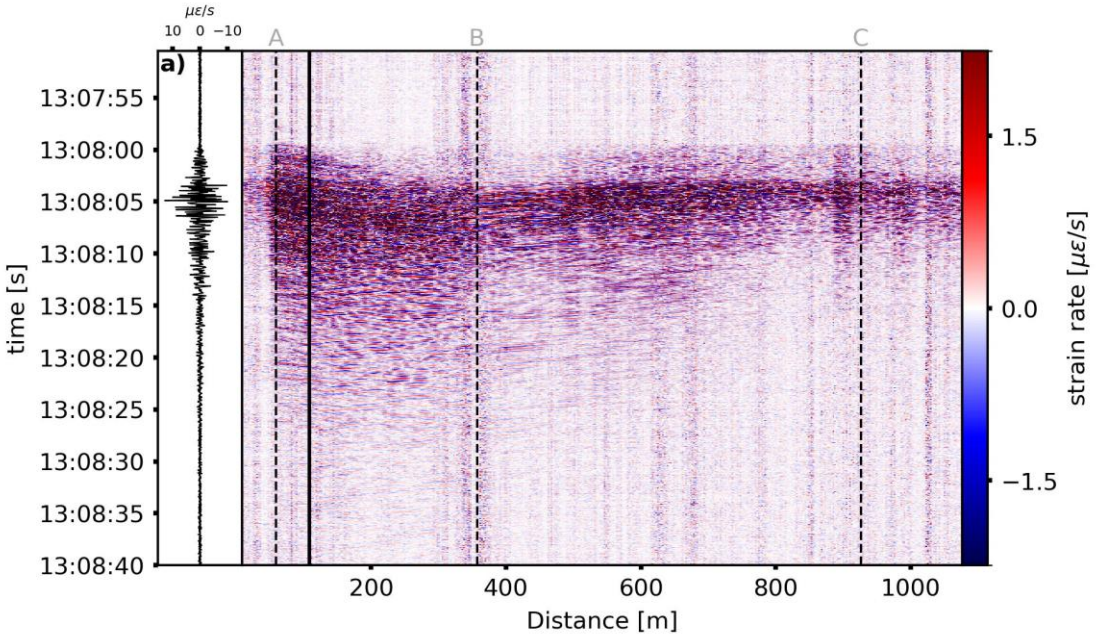

Figure 5*:* The space-time representation of the strain rate wavefield, filtered between 1 and 30 Hz, recorded by the DAS system for a M_L2.3 event occurred on 2021/09/20. The black filled line marks the channel, whose time signal is shown on the left side, while the dashed black lines individuate specific points along the cable, shown in Figure 4b.

For this dataset, we restricted the source parameters estimation to channels satisfying SNR>8, resulting into a catalog of 26 events that meet the SNR criterion at a minimum number of 40 channels. This curated dataset (Figure 4a) includes events with local magnitude spanning from 0.4 up to 2.3, and hypocentral distances from $6km$ to $60km$ (see Data and Availability statement for complete catalog information; magnitude and distance distribution of the events is represented in Figure S8b) Amplitude spectra were computed on 5s time windows around the S-pick (from 0.5s before to 4.5s after the S-pick), this latter obtained from the nearby station (COL3, distance from the fiber < $2km$, see Figure 4b).

By analyzing the spectra of the events along the fiber, we observed that the spectral decay following the plateau level starts around an apparent corner frequency of $5.5Hz$ (grey circles,

Figure 6b), irrespective of the event magnitude and location and of the channel along the fiber (Figure 6a). The saturation of the apparent corner frequency and the following decay can be ascribed to local site effects (e.g., Hanks, 1982) because spectral fall-offs due to the source and to the anelastic attenuation are both expected to show a cut-off frequency dependent on magnitude (source corner frequency) and distance (regional anelastic attenuation; eq. (7)). Moreover, assuming an average value of the quality factor Q for the area ($Q = 230$; Zollo et al., 2014; Amoroso et al., 2017) the spectral decay due to the anelastic attenuation is generally expected to start at frequencies higher than $5.5Hz$ for the range of hypocentral distances associated with events recorded at the fiber.

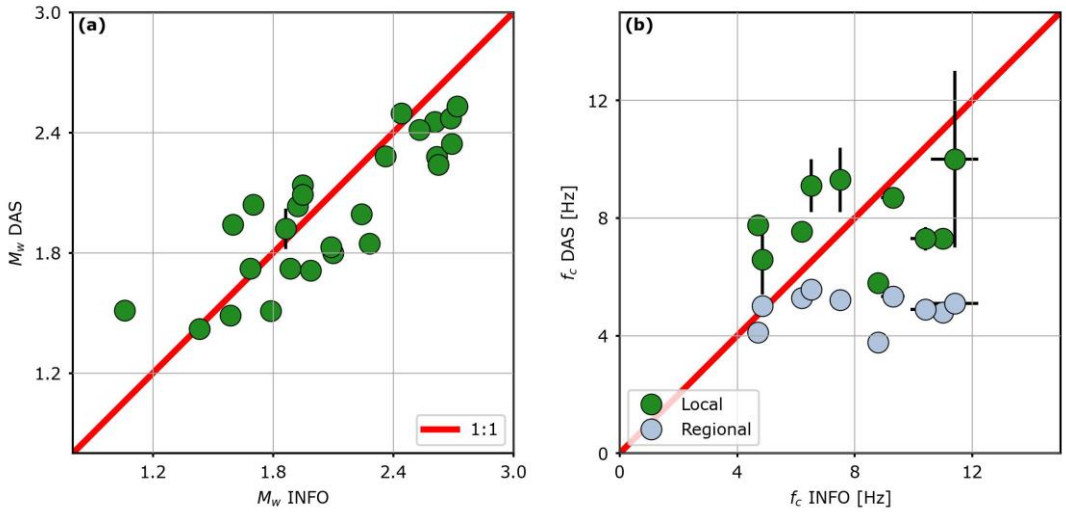

Figure 6: (a) Moment magnitude comparison between estimates from DAS and from INFO network. Estimates from DAS data follow a 1:1 scaling (red line) when compared with standard seismic station results. **(b)** Corner frequency comparison between DAS and local network. Without correction for local site effects (gray dots) DAS estimates saturate resulting into an apparent f_c around $5.5Hz$. After the correction for local site effects (green dots), the two estimates become comparable.

We modelled the local site effects using the local attenuation coefficient k^c, as described in eq. (10) (Anderson & Hough, 1984; Butcher et al., 2020; Ktenidou et al., 2014, 2015). To infer an average value for k^c, we selected small magnitude events in the dataset ($M_w < 2.0$) for which the source corner frequency is expected to be much larger than the observed cut-off frequency (Zollo et al., 2014). For these events, after removal of regional anelastic attenuation assuming $Q = 230$, we fit the logarithm of the amplitude spectra as a function of the frequency to evaluate k^c for each channel and each event (Figure 7a). In Figure 7b, we represent the spatial variability of k^c along the fiber. The local attenuation coefficient has its maximum in the central

section of the cable, decreasing almost linearly toward the ends of the cable, and possibly mimicking the shape of the lake basement. We computed the median and the SMAD values from k^c single-channel averages, leading to $\bar{k}^c = (0.08 \pm 0.02)$s.

Since the k^c estimates are not available or they are not equally robust at all channels, due to the coupling and rapid changes in direction of the cable, the median value was used in the source inversion of the largest magnitude events ($M_w > 2.0$) to remove local site effects from their observed spectra, thereby evaluating their seismic moment and source corner frequency.

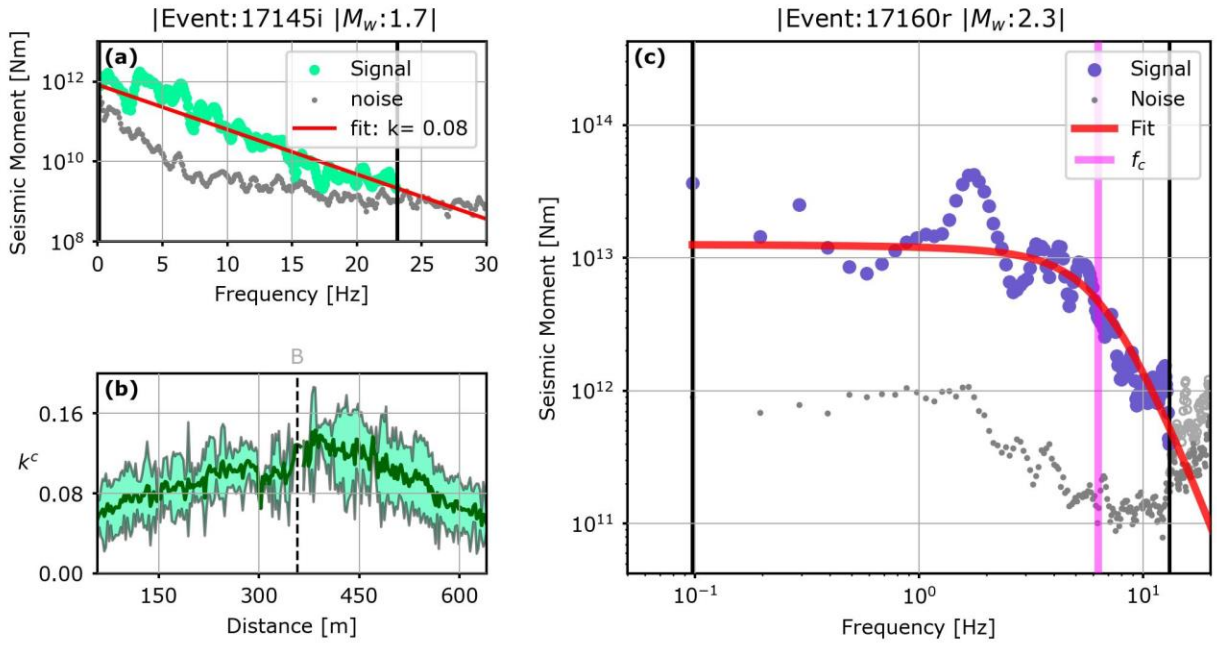

Figure 7*:* (a) Example of the linear fit (red curve) estimated on the log-linear spectrum (green circles) of one of the smallest events in the dataset ($M_w < 2.0$) at a specific channel of the fiber to obtain a single-channel estimate of k^c. The spectrum is fitted in the frequency band where the SNR exceeds the imposed threshold of 3.5 (black vertical bars). **(b)** k^c variability along the cable represented by the mean (blue green curve) and standard deviation (shaded area). The dashed black line individuates the position where the cable has a kink (Figure 4b). **(c)** Log-log spectrum at one channel for a M_w2.3 event after the site contribution was removed using the averaged value of k^c along the cable. The image has the same color code described in Figure 1. The f_c estimation is marked by a vertical magenta line. (Time traces of the two events are shown in Supplementary Information Text S10).

We compared source parameters estimation from DAS and INFO network seismic records (Figure 6). M_w estimations from DAS were found to be consistent in the analyzed magnitude range with the ones retrieved from the INFO network, obtained inverting local seismic records (Fig. 6a). The correlation between both estimates is lower than in the Chilean

401 case. For Southern Apennines, this can be attributed to the short length of the cable that does not
402 capture the variability of the M_w estimates due the distance and azimuth. Corner frequencies
403 recovered from DAS saturate at 5.5 Hz without the site correction (gray dots, Figure 6b) but are
404 compatible with the ones obtained from INFO seismic stations when modelling the site
405 attenuation for the largest events (green dots, Figure 6b).
406

407 **4 Discussions**

408 The new formulation of the far field strain spectra developed in this work does not
409 require to convert waveforms from strain to velocity (e.g., Wang et al., 2018; Lior et al., 2021;
410 Trabattoni et al., 2023) and can be directly applied to raw DAS data. Signal manipulation during
411 the conversion to kinematic quantities could modify the seismic spectra. For example, the low-
412 wavenumber accuracy of the conversion of the strain rate to displacement by direct integration is
413 limited by the rectilinearity of the fiber (Trabattoni et al., 2023). Also, the use of the slant-stack
414 transform for the evaluation of the dominant apparent velocity (Lior et al., 2021, 2023), only
415 allows to correctly convert the most energetic phase, and the spurious contribution of other not
416 well-integrated, superimposing phases, cannot be easily evaluated. The proposed strategy also
417 disengages from the colocation hypothesis and the knowledge of parameters for a reference
418 event, as required for EGF based approaches (Chen, 2023) that also rely on raw DAS data.

419 From the theoretical formulation, we retrieve an enhanced sensitivity of strain
420 measurements to the shallow structure beneath the cable, with a dependence on the wave
421 velocity at three-halves power instead of one-half, as compared to the displacement formulation.
422 Knowledge of a-priori shallow S (and P) wave velocities is thus relevant to avoid biases in the
423 estimation of the seismic moment. It is worth to note that this velocity also enters (as apparent
424 velocity) in the conversion from strain-rate to acceleration (Daley et al., 2016).

425 We also report average radiation pattern contributions which are more than twice smaller
426 than the ones retrieved for seismometer records, in agreement to the lower and complex
427 directional sensitivity of DAS to body waves (Martin et al., 2021). Moreover, the presence of
428 additional nodes in the radiation pattern diagrams suggests cable deployments with changes in
429 the fiber orientation, to improve the resolution in the source parameters.

Finally, the proposed approach, when integrated in a probabilistic formulation, can be fully automated, with the quality of the solutions based on the shape of the a-posteriori probability density functions (Supino et al., 2019). Also, when extending this approach to the P-waves, this strategy could be applied in real-time, when few seconds of early P wave signal are available (e.g., Caprio et al., 2011).

Validation of this approach on Chilean dataset ($M_L = 2.6 - 4.3$) shows a reliable estimation of source parameters, comparable with results from standard seismometers. We do not observe any dependence of parameters on the hypocentral distance, enabling DAS to characterize the source of events in wide range of hypocentral distances. Moreover, source parameters exhibit scale invariant stress drop with an average value of $(0.8 \pm 0.6) MPa$, consistent with the values retrieved for events in Central Chile.

In the second application we analyzed smaller size events ($M_L = 0.4 - 2.3$), using DAS data recorded on a much shorter ($1.1 km$) cable installed in the active tectonic environment of Southern Apennines (Italy). We found good agreement for moment magnitude estimates from DAS as compared to the ones from standard seismic stations in the explored magnitude range. Because of the specific installation site (a dry lake), local attenuation plays a crucial role, masking the effect of the source size in the spectrum. Using a parametric EGF-based approach, we estimated an average local attenuation coefficient $\bar{k}^c = (0.08 \pm 0.02)$ s that is comparable with the values estimated in very soft soils (Ktenidou et al., 2015). Also, the analysis of the variability of k^c shows linear trends with distance along the cable, coherent with the increase in attenuation with the distances from the tips of the basin (Trabattoni et al., 2022), and that can be correlated with the depth of the structure (Campbell, 2009). When removing this attenuation from the spectra of the largest magnitude events in the catalog ($M_w > 2$), we were able to resolve the corner frequencies, that now result to be coherent with the estimates from velocity seismograms.

The estimation of the k^c parameter for the Southern Italy dataset indicates the possibility to use DAS data to infer mechanical properties of the shallow layering, beyond the source parameters when the site-associated spectral cut-off occurs in the central part of the available frequency band for the inversion. This condition does not apply for the Chilean data, where we report no saturation of the corner frequency for the analyzed set of events.

Epistemic uncertainty associated with regional attenuation, corrected by a frequency independent quality factor, site effects described through the k^c parameter, and average radiation pattern coefficients may result in an increase of the variability of source parameters along the fiber.

When analyzing the residuals in source parameter estimation, we did not observe any dependence on the distance, indicating a consistent description of the associated amplitude decay. Frequency dependent site effects along the cable would be more difficult to analyze, since they depend on the orientation of the fiber and the backazimuth of the events. Larger datasets and complementary analysis, grounded on ambient noise and simulations, are required to relate these effects to the morphology and velocity of the shallow layers (Bordoni et al., 2011).

Moreover, to take advantage of distributed estimations obtained through DAS, after correction for attenuation and site, investigating residuals along the cable can bring information on the variability of the radiation pattern, that can be used to constrain the focal mechanisms of the events, in addition to polarities (Zahradník et al., 2001).

Working with DAS spectral amplitudes, especially for time integrated strain data, displays unique instrumental noise, with coherent low frequency contribution that tightens the bandwidth where the signal can be inverted (Lior et al., 2023). This issue is related to instrumental properties and unwrapping errors rather than seismic information in the signal, and could be mitigated with the ongoing evolution and increasing demand of distributed sensing sensors. However, for events for which we estimated both seismic moment and event size (M_w between 2.0 and 4.3) we report that the corner frequency lies in the middle of the frequency band available for the inversion, allowing for an accurate estimation of source parameters as it is demonstrated by the comparison with results from standard seismic instruments. For smaller magnitude events, we were able to capture only the flat level of the spectrum, preventing from the estimate of earthquake size. We might also expect a limitation in the use of DAS data for source parameter estimation for events with magnitude larger than $4.5 - 5.0$ (not included in the analyzed catalogs), where the expected corner frequency approaches the lower limit of the informative frequency bandwidth. In this case, the inversion could provide biased estimates for the moment magnitude, as compared to standard instruments.

Consistency of estimates between DAS and seismic data guarantees that the contribution of secondary phases in the selected S-wave window, to which the DAS could be more sensitive, does not introduce significant biases in the retrieved source parameters.

5 Conclusions

In this work we estimated source parameters from a spectral inversion of DAS data in their native representation, based on a novel formulation describing the far-field radiation in the strain domain. The theoretical modeling displays an enhanced sensitivity to the velocity structure beneath the cable and the radiation pattern.

Including this model in a probabilistic framework for the inversion (Supino et al., 2019) allowed us to estimate the moment magnitude and the corner frequency from two different datasets, showing consistent values when compared to authoritative catalogs.

When analyzing data acquired from a $150km$ ocean-bottom dark fiber cable near the Chilean trench ($M_L = 2.6 - 4.3$), we found near to constant stress drop, with an average estimate of $0.8 \pm 0.6MPa$. Despite their natural variability, we report no biases of average estimations of source parameters with hypocentral distance along the cable.

Application of the technique to microseismic data ($M_L = 0.3 - 2.3$) acquired in the Southern Apennines (Italy) represent a challenging test for the achievable resolution in the characterization of small earthquakes using DAS. We coherently estimated the seismic moment in the whole magnitude interval. Site effects were shown to dominate the high frequency part of the spectrum and need to be modelled and corrected for to retrieve the source extension for events with $M_w > 2$.

The two case studies presented in this work reveal the high potential of DAS for source characterization, while the dense spatial sampling could be a key ingredient for understanding source parameters variability and their relationship with the rupture behavior and the local structure. Nonetheless, fiber optic data require careful processing both for the peculiar signal properties, and for the large amount of information necessitating efficient storage and handling procedures.

Acknowledgments

We are grateful to two anonymous reviewers and the editor for their comments. This work has been supported by the EU project Geo-Inquire, funded by the European Commission under project number 101058518 within the HORIZON-INFRA-2021-SERV-01 call. Chilean data have been retrieved in the framework of the project funded by the European Research Council (ERC) under the European Union's Horizon 2020 research and innovation programme (grant agreement No. 101041092).

Data Availability Statement

The strain rates of the Chilean earthquakes used in this article are available at the link: https://doi.org/10.5281/zenodo.8340063 (Rivet et al., 2023). DAS waveforms from the Southern Apennines dataset are available at: https://doi.org/10.5281/zenodo.8337580 (Strumia et al., 2023(b)). Seismic data from Chilean seismic station can be downloaded through the EarthScope Consortium Wilber 3 system (https://ds.iris.edu/wilber3/) or EarthScope Consortium Web Services (https://service.iris.edu/), network code C1 (Universidad de Chile, 2012). Products from INFO network can be accessed through the Irpinia Seismic Network infrastructure (ISNet: https://isnet.unina.it). Seismic data can be accessed through EIDA portal (https://eida.ingv.it/it/), network code IX.

Catalogs of the analyzed events are available at the following link: https://doi.org/10.5281/zenodo.10119097 (Strumia et al., 2023(c)).

Codes used to produce the Figures in the paper can be found here: https://doi.org/10.5281/zenodo.10157509 (Strumia et al., 2023(a)).

Figures were made using matplotlib version 3.6.3. Maps in Figure 4 and Figure S3 was made using PyGMT (Uieda et al., 2021) using Generic Mapping Tools (GMT) version 6 (Wessel et al., 2019).

References

Abercrombie, R. E. (1995). Earthquake source scaling relationships from −1 to 5 ML using seismograms recorded at 2.5-km depth. *Journal of Geophysical Research: Solid Earth*, *100*(B12), 24015–24036. https://doi.org/10.1029/95JB02397

Abercrombie, R. E., Bannister, S., Ristau, J., & Doser, D. (2017). Variability of earthquake stress drop in a subduction setting, the Hikurangi Margin, New Zealand. *Geophysical Journal International*, *208*(1), 306–320. https://doi.org/10.1093/gji/ggw393

Abercrombie, R. E., & Rice, J. R. (2005). Can observations of earthquake scaling constrain slip weakening? In *Geophysical Journal International* (Vol. 162, Issue 2, pp. 406–424). https://doi.org/10.1111/j.1365-246X.2005.02579.x

Abercrombie Rachel E. 2021Resolution and uncertainties in estimates of earthquake stress drop and energy release. Phil. Trans. R. Soc. A.379: 20200131. 20200131. https://doi.org/10.1098/rsta.2020.0131

Ajo-Franklin, J. B., Dou, S., Lindsey, N. J., Monga, I., Tracy, C., Robertson, M., Rodriguez Tribaldos, V., Ulrich, C., Freifeld, B., Daley, T., & Li, X. (2019). Distributed Acoustic Sensing Using Dark Fiber for Near-Surface Characterization and Broadband Seismic Event Detection. *Scientific Reports*, *9*(1). https://doi.org/10.1038/s41598-018-36675-8

Aki, K., & Richards, P. G. (2002). *Quantitative seismology*.

Amoroso, O., Russo, G., De Landro, G., Zollo, A., Garambois, S., Mazzoli, S., Parente, M., & Virieux, J. (2017). From velocity and attenuation tomography to rock physical modeling: Inferences on fluid-driven earthquake processes at the Irpinia fault system in southern Italy. *Geophysical Research Letters*, *44*(13), 6752–6760. https://doi.org/10.1002/2016GL072346

Anderson, J. G., & Hough, S. E. (1984). A model for the shape of the Fourier amplitude spectrum of acceleration at high frequencies. In *Bulletin of the Seismological Society of America* (Vol. 74, Issue 5).

Arthur H. Hartog. (2017). *An introduction to distributed optical fibre sensors* (A. H. Hartog, Ed.). CRC Press.

Baltay, A. S., & Hanks, T. C. (2014). Understanding the magnitude dependence of PGA and PGV in NGA-West 2 data. In *Bulletin of the Seismological Society of America*, 104(6), 2851-2865. https://doi.org/10.1785/0120130283

Boore, D. M., & Boatwright, J. (1984). Average body-wave radiation coeffiecients. In *Bulletin of the Seismological Society of America* (Vol. 74, Issue 5).

Bordoni, P., Haines, J., Milana, G., Marcucci, S., Cara, F., & Di Giulio, G. (2011). Seismic response of L'Aquila downtown from comparison between 2D synthetics spectral

ratios of SH, P-SV and Rayleigh waves and observations of the 2009 earthquake sequence. *Bulletin of Earthquake Engineering*, 9, 761-781. https://doi.org/10.1007/s10518-011-9247-5

Brune, J. N. (1970). Tectonic stress and the spectra of seismic shear waves from earthquakes. *Journal of Geophysical Research*, *75*(26), 4997–5009. https://doi.org/10.1029/JB075i026p04997

Butcher, A., Luckett, R., Kendall, J. M., & Baptie, B. (2020). Seismic magnitudes, corner frequencies, and microseismicity: Using ambient noise to correct for high-frequency attenuation. *Bulletin of the Seismological Society of America*, *110*(3), 1260–1275. https://doi.org/10.1785/0120190032

Campbell, K. W. (2009). Estimates of Shear-Wave Q and κ0 for unconsolidated and semiconsolidated sediments in Eastern North America. *Bulletin of the Seismological Society of America*, *99*(4), 2365–2392. https://doi.org/10.1785/0120080116

Caprio, M., Lancieri, M., Cua, G. B., Zollo, A., & Wiemer, S. (2011). An evolutionary approach to real-time moment magnitude estimation via inversion of displacement spectra. *Geophysical Research Letters*, *38*(2). https://doi.org/10.1029/2010GL045403

Chen, X. (2023). Source parameter analysis using distributed acoustic sensing - an example with the PoroTomo array. *Geophysical Journal International*, *233*(3), 2207–2213. https://doi.org/10.1093/gji/ggad061

Chiaraluce, L., Festa, G., Bernard, P., Caracausi, A., Carluccio, I., Clinton, J. F., Di Stefano, R., Elia, L., Evangelidis, C. P., Ergintav, S., Jianu, O., Kaviris, G., Marmureanu, A., Šebela, S., & Sokos, E. (2022). The Near Fault Observatory community in Europe: a new resource for faulting and hazard studies. *Annals of Geophysics*, *65*(3), 1–17. https://doi.org/10.4401/ag-8778

Currenti, G., Jousset, P., Napoli, R., Krawczyk, C., & Weber, M. (2021). On the comparison of strain measurements from fibre optics with a dense seismometer array at Etna volcano (Italy). *Solid Earth*, *12*(4), 993–1003. https://doi.org/10.5194/se-12-993-2021

Daley, T. M., Miller, D. E., Dodds, K., Cook, P., & Freifeld, B. M. (2016). Field testing of modular borehole monitoring with simultaneous distributed acoustic sensing and

geophone vertical seismic profiles at Citronelle, Alabama. *Geophysical Prospecting*, *64*(5), 1318–1334. https://doi.org/10.1111/1365-2478.12324

Hanks, T. C. (1982). f max. *Bulletin of the Seismological Society of America* 1982; 72 (6A): 1867–1879. https://doi.org/10.1785/BSSA07206A1867

Haskell, N. A. (1964). Total energy and energy spectral density of elastic wave radiation from propagating faults. *Bulletin of the Seismological Society of America*, *54*(6A), 1811–1841. https://doi.org/10.1785/BSSA05406A1811

Kaneko, Y., & Shearer, P. M. (2014). Seismic source spectra and estimated stress drop derived from cohesive-zone models of circular subshear rupture. *Geophysical Journal International*, *197*(2), 1002–1015. https://doi.org/10.1093/gji/ggu030

Keylis-Borok, V. (1959). On estimation of the displacement in an earthquake source and of source dimensions. *Annals of Geophysics*, *12*(2).

Ktenidou, O. J., Abrahamson, N. A., Drouet, S., & Cotton, F. (2015). Understanding the physics of kappa (κ): Insights from a downhole array. *Geophysical Journal International*, *203*(1), 678–691. https://doi.org/10.1093/gji/ggv315

Ktenidou, O. J., Cotton, F., Abrahamson, N. A., & Anderson, J. G. (2014). Taxonomy of κ: A review of definitions and estimation approaches targeted to applications. *Seismological Research Letters*, *85*(1), 135–146. https://doi.org/10.1785/0220130027

Lellouch, A., Lindsey, N. J., Ellsworth, W. L., & Biondi, B. L. (2020). Comparison between distributed acoustic sensing and geophones: Downhole microseismic monitoring of the FORGE geothermal experiment. *Seismological Research Letters*, *91*(6), 3256–3268. https://doi.org/10.1785/0220200149

Lellouch, A., Yuan, S., Spica, Z., Biondi, B., & Ellsworth, W. L. (2019). Seismic Velocity Estimation Using Passive Downhole Distributed Acoustic Sensing Records: Examples From the San Andreas Fault Observatory at Depth. *Journal of Geophysical Research: Solid Earth*, *124*(7), 6931–6948. https://doi.org/10.1029/2019JB017533

Li, J., Zhu, W., Biondi, E., & Zhan, Z. (2023). Earthquake focal mechanisms with distributed acoustic sensing. *Nature Communications*, *14*(1), 4181. https://doi.org/10.1038/s41467-023-39639-3

Lior, I., Rivet, D., Ampuero, J. P., Sladen, A., Barrientos, S., Sánchez-Olavarría, R., Villarroel Opazo, G. A., & Bustamante Prado, J. A. (2023). Magnitude estimation and

ground motion prediction to harness fiber optic distributed acoustic sensing for earthquake early warning. *Scientific Reports*, *13*(1). https://doi.org/10.1038/s41598-023-27444-3

Lior, I., Sladen, A., Mercerat, D., Ampuero, J. P., Rivet, D., & Sambolian, S. (2021). Strain to ground motion conversion of distributed acoustic sensing data for earthquake magnitude and stress drop determination. *Solid Earth*, *12*(6), 1421–1442. https://doi.org/10.5194/se-12-1421-2021

Madariaga, R. (1976). Dynamics of an expanding circular fault. *Bulletin of the Seismological Society of America*, *66*(3), 639–666. https://doi.org/10.1785/bssa0660030639

Marot, M., Monfret, T., Gerbault, M., Nolet, G., Ranalli, G., & Pardo, M. (2014). Flat versus normal subduction zones: A comparison based on 3-D regional traveltime tomography and petrological modelling of central Chile and western Argentina (29°-35°S). *Geophysical Journal International*, *199*(3), 1633–1654. https://doi.org/10.1093/gji/ggu355

Martin, E. R., Lindsey, N. J., Ajo-Franklin, J. B., & Biondi, B. L. (2021). Introduction to Interferometry of Fiber-Optic Strain Measurements. In *Distributed Acoustic Sensing in Geophysics: Methods and Applications* (pp. 113–129). wiley. https://doi.org/10.1002/9781119521808.ch09

Mousavi, S. M., Ellsworth, W. L., Zhu, W., Chuang, L. Y., & Beroza, G. C. (2020). Earthquake transformer—an attentive deep-learning model for simultaneous earthquake detection and phase picking. *Nature Communications*, *11*(1). https://doi.org/10.1038/s41467-020-17591-w

Nishimura, T., Emoto, K., Nakahara, H., Miura, S., Yamamoto, M., Sugimura, S., Ishikawa, A., & Kimura, T. (2021). Source location of volcanic earthquakes and subsurface characterization using fiber-optic cable and distributed acoustic sensing system. *Scientific Reports*, *11*(1). https://doi.org/10.1038/s41598-021-85621-8

Oth, A., Bindi, D., Parolai, S., & Wenzel, F. (2007). *S-Wave Attenuation Characteristics Beneath the Vrancea Region (Romania)-New Insights from the Inversion of Ground Motion Spectra*.

669 Papp, B., Donno, D., Martin, J. E., & Hartog, A. H. (2017). A study of the geophysical
670 response of distributed fibre optic acoustic sensors through laboratory-scale
671 experiments. *Geophysical Prospecting*, *65*(5), 1186–1204.
672 https://doi.org/10.1111/1365-2478.12471
673 Piana Agostinetti, N., Villa, A., & Saccorotti, G. (2022). Distributed acoustic sensing as a
674 tool for subsurface mapping and seismic event monitoring: A proof of concept. *Solid*
675 *Earth*, *13*(2), 449–468. https://doi.org/10.5194/se-13-449-2022
676 Prieto, G. A., Shearer, P. M., Vernon, F. L., & Kilb, D. (2004). Earthquake source scaling
677 and self-similarity estimation from stacking P and S spectra. *Journal of Geophysical*
678 *Research: Solid Earth*, *109*(8). https://doi.org/10.1029/2004JB003084
679 Rivet, D., Trabattoni, A., & Baillet, M. (2023). DAS Chile waveforms [Data set]. Zenodo.
680 https://doi.org/10.5281/zenodo.8340063
681 Sato T., & Hirasawa, T. (1973). Body wave spectra from propagating shear cracks. *Journal*
682 *of Physics of the Earth*, 21(4), 415-431.
683 Scotto di Uccio, F., Scala, A., Festa, G., Picozzi, M., & Beroza, G. C. (2023). Comparing
684 and integrating artificial intelligence and similarity search detection techniques:
685 application to seismic sequences in Southern Italy. *Geophysical Journal International*,
686 *233*(2), 861–874. https://doi.org/10.1093/gji/ggac487
687 Şen, A. T., Cesca, S., Lange, D., Dahm, T., Tilmann, F., & Heimann, S. (2015). Systematic
688 Changes of Earthquake Rupture with Depth: A Case Study from the 2010 Mw8.8
689 Maule, Chile, Earthquake Aftershock Sequence. *Bulletin of the Seismological Society*
690 *of America*, *105*(5), 2468–2479. https://doi.org/10.1785/0120140123
691 Sladen, A., Rivet, D., Ampuero, J. P., De Barros, L., Hello, Y., Calbris, G., & Lamare, P.
692 (2019). Distributed sensing of earthquakes and ocean-solid Earth interactions on
693 seafloor telecom cables. *Nature Communications*, *10*(1).
694 https://doi.org/10.1038/s41467-019-13793-z
695 Spica, Z. J., Perton, M., Martin, E. R., Beroza, G. C., & Biondi, B. (2020). Urban Seismic
696 Site Characterization by Fiber-Optic Seismology. *Journal of Geophysical Research:*
697 *Solid Earth, 125*(3). https://doi.org/10.1029/2019JB018656
698 Strumia, C. (2023). DAS for source characterization – Figures [Software]. Zenodo.
699 https://doi.org/10.5281/zenodo.10157509

Strumia, C., Festa, G., & Trabattoni, A. (2023). DAS Irpinia waveforms [Data set]. Zenodo. https://doi.org/10.5281/zenodo.8337580

Strumia, C., & Marie, B. (2023). Earthquake source characterization with DAS - catalogs [Data set]. Zenodo. https://doi.org/10.5281/zenodo.10119097

Supino, M., Festa, G., & Zollo, A. (2019). A probabilistic method for the estimation of earthquake source parameters from spectral inversion: Application to the 2016-2017 Central Italy seismic sequence. *Geophysical Journal International*, *218*(2), 988–1007. https://doi.org/10.1093/gji/ggz206

Tarantola, A. (2004). *Inverse Problem Theory and Methods for Model Parameter Estimation*.

Trabattoni, A., Biagioli, F., Strumia, C., Van Den Ende, M., Scotto Di Uccio, F., Festa, G., Rivet, D., Sladen, A., Ampuero, J. P., Métaxian, J.-P., & Stutzmann, É. (2023). From strain to displacement: using deformation to enhance distributed acoustic sensing applications, Geophysical Journal International, 235(3), 2372–2384. https://doi.org/10.1093/gji/ggad365

Trabattoni, A., Festa, G., Longo, R., Bernard, P., Plantier, G., Zollo, A., & Strollo, A. (2022). Microseismicity Monitoring and Site Characterization With Distributed Acoustic Sensing (DAS): The Case of the Irpinia Fault System (Southern Italy). *Journal of Geophysical Research: Solid Earth*, *127*(9). https://doi.org/10.1029/2022JB024529

Trifunac, M. D., & Brady, A. G. (1975). A study on the duration of strong earthquake ground motion. In *Bulletin of the Seismological Society of America* (Vol. 65, Issue 3).

Tsuji, T., Ikeda, T., Matsuura, R., Mukumoto, K., Hutapea, F. L., Kimura, T., Yamaoka, K., & Shinohara, M. (2021). Continuous monitoring system for safe managements of CO2 storage and geothermal reservoirs. *Scientific Reports*, *11*(1). https://doi.org/10.1038/s41598-021-97881-5

Uieda, L., Tian, D., Leong, W. J., Toney, L., Schlitzer, W., Yao, J., Grund, M., Jones, M., Materna, K., Newton, T., Ziebarth, M., & Wessel, P. (2021). PyGMT: A Python interface for the Generic Mapping Tools (v0.3.1) [Software]. Zenodo. https://doi.org/10.5281/zenodo.4592991

Universidad de Chile. (2012). *Red Sismologica Nacional* [Data set]. International Federation of Digital Seismograph Networks. https://doi.org/10.7914/SN/C1

Van Den Ende, M. P. A., & Ampuero, J. P. (2021). Evaluating seismic beamforming capabilities of distributed acoustic sensing arrays. *Solid Earth*, *12*(4), 915–934. https://doi.org/10.5194/se-12-915-2021

Wang, H. F., Zeng, X., Miller, D. E., Fratta, D., Feigl, K. L., Thurber, C. H., & Mellors, R. J. (2018). Ground motion response to an ML 4.3 earthquake using co-located distributed acoustic sensing and seismometer arrays. *Geophysical Journal International*, *213*(3), 2020–2036. https://doi.org/10.1093/GJI/GGY102

Wessel, P., Luis, J. F., Uieda, L., Scharroo, R., Wobbe, F., Smith, W. H. F., & Tian, D. (2019). The Generic Mapping Tools Version 6. *Geochemistry, Geophysics, Geosystems*, *20*(11), 5556–5564. https://doi.org/10.1029/2019GC008515

Yin, J., Zhu, W., Li, J., Biondi, E., Miao, Y., Spica, Z. J., Viens, L., Shinohara, M., Ide, S., Mochizuki, K., Husker, A. L., & Zhan, Z. (2023). Earthquake Magnitude With DAS: A Transferable Data-Based Scaling Relation. *Geophysical Research Letters*, *50*(10). https://doi.org/10.1029/2023GL103045

Zahradník, J., Janský, J., & Papatsimpa, K. (2001). Focal mechanisms of weak earthquakes from amplitude spectra and polarities. *Pure and Applied Geophysics*, 158, 647-665. https://doi.org/10.1007/PL00001198

Zhu, W., McBrearty, I. W., Mousavi, S. M., Ellsworth, W. L., & Beroza, G. C. (2022). Earthquake Phase Association Using a Bayesian Gaussian Mixture Model. *Journal of Geophysical Research: Solid Earth*, *127*(5). https://doi.org/10.1029/2021JB023249

Zollo, A., Orefice, A., & Convertito, V. (2014). Source parameter scaling and radiation efficiency of microearthquakes along the Irpinia fault zone in southern Apennines, Italy. *Journal of Geophysical Research: Solid Earth*, *119*(4), 3256–3275. https://doi.org/10.1002/2013JB010116

Supporting Information summary

Text S1 to S10

Figures S1 to S9

761

762 **References from the supporting information**

763 Boore, D. M., & Boatwright, J. (1984). Average body-wave radiation coeffiecients. In
764 *Bulletin of the Seismological Society of America* (Vol. 74, Issue 5).

765 Mousavi, S. M., Ellsworth, W. L., Zhu, W., Chuang, L. Y., & Beroza, G. C. (2020).
766 Earthquake transformer—an attentive deep-learning model for simultaneous
767 earthquake detection and phase picking. *Nature Communications*, *11*(1).
768 https://doi.org/10.1038/s41467-020-17591-w

769 Trabattoni, A., Biagioli, F., Strumia, C., Van Den Ende, M., Scotto Di Uccio, F., Festa, G.,
770 Rivet, D., Sladen, A., Ampuero, J. P., Métaxian, J.-P., & Stutzmann, É. (2023).
771 From strain to displacement: using deformation to enhance distributed acoustic
772 sensing applications, Geophysical Journal International, 235(3), 2372–
773 2384. https://doi.org/10.1093/gji/ggad365

774 Trifunac, M. D., & Brady, A. G. (1975). A study on the duration of strong earthquake
775 ground motion. In *Bulletin of the Seismological Society of America* (Vol. 65, Issue
776 3).

777 Zhu, W., McBrearty, I. W., Mousavi, S. M., Ellsworth, W. L., & Beroza, G. C. (2022).
778 Earthquake Phase Association Using a Bayesian Gaussian Mixture Model. *Journal*
779 *of Geophysical Research: Solid Earth*, *127*(5).
780 https://doi.org/10.1029/2021JB023249

781